Magnon blockade in a QED system with a giant spin ensemble and a giant atom coupled to a waveguide

Xin Wang, Kai-Wei Huang, and Hao Xiong[*]
School of Physics, Huazhong University of Science and Technology, Wuhan, Hubei 430074, China

(Received 21 May 2024; revised 6 August 2024; accepted 22 August 2024; published 4 September 2024)

We propose a scheme to achieve the magnon blockade (MB) effect in a system consisting of a giant spin ensemble and a giant atom coupled to a waveguide. We show a physical mechanism for generating the MB through non-Hermitian anharmonicity. The non-Hermitian magnon blockade (NHMB) is realized in braided, nested, and separate coupling configurations. The NHMB is shown to be useful for the preparation of a high-efficiency and high-purity single magnon. Remarkably, the coexistence phenomenon of the conventional magnon blockade and the unconventional magnon blockade occurs and their conversion can be completed in the braided and nested coupling configurations. This result realizes the modulation between efficiency and purity of single-magnon generation. For the separate coupling configuration, the frequency-tunable NHMB is obtained due to the variation of Lamb shifts. The phase caused by the photon propagating between neighboring coupling points offers a simple and flexible method to modulate the conversion of MB effects induced by multiple physical mechanisms. Our results open a pathway to manipulate the generation of the MB on demand, which has potential applications in producing a single-magnon source and performing magnon-based quantum information processing.

DOI: 10.1103/PhysRevA.110.033702

I. INTRODUCTION

Magnons, quanta of collective spin excitations in ferromagnetic crystals, have attracted extensive attention and have become suitable candidates for carriers of quantum information due to their unique physical advantages including long lifetime, excellent compatibility, and widespread frequency tunability [1,2]. The magnon mode can couple to other quantum information carriers including microwave photons, optical photons, superconducting qubits, and mechanical phonons [3–9]. These offer a building block for constructing hybrid quantum systems. Multiple exotic physical phenomena [10–14] have been investigated in hybrid magnonic system. In particular, as a pure quantum effect, the magnon blockade (MB) [15–29], which is analogous to the photon blockade [30–38] and phonon blockade [39,40], can be useful for single-magnon preparation and make the quantum control at the level of a single magnon possible.

Recently, the study of the giant atom (GA), as an emerging field in the quantum optical paradigm, has been able to achieve the nonlocal light-matter interaction since the GA can couple to the waveguide at multiple separate points. The interference effect between multiple coupling points in waveguide quantum electrodynamics (QED) systems containing GAs can result in a series of intriguing phenomena, such as frequency-dependent relaxation rates and Lamb shifts [41], decoherence-free interaction [42,43], non-Markovian collective radiance [44], bound states [45–47], advanced photonic manipulation [48–53], and GA entanglement [54,55]. It has been demonstrated that the GA can be realized in superconducting quantum circuits [56–59], cold atoms in optical lattices [60], and a synthetic frequency dimension [61]. Meanwhile, the waveguide magnon system is responsible for remote quantum magnon control [62–66] since the waveguide can be used as the transmission channel for the quantum information carrier. Magnon-photon, magnon-magnon, and magnon-qubit dissipative couplings [21,67–70] have been proved based on the waveguide magnon system, which is a physical architecture for studying the non-Hermitian property in the area of magnon spintronics. Benefiting from the development of the waveguide magnon system, in analogy to the GA, the giant spin ensemble (GSE) has been constructed through coupling the ferromagnetic spin ensemble to a meandering waveguide at two coupling located points [71] and nonreciprocal single-photon scattering based on the GSE waveguide has been reported [72], which provides an ideal platform for exploring quantum information manipulation.

In this work we combine the GSE and the GA together in a common waveguide to study the properties of the MB. Recently, the investigation of the photon blockade entered the non-Hermitian domain [73–75]. In particular, a physical mechanism for generating the photon blockade was proposed where the anharmonicity of energy levels is replaced by anharmonic dissipation. The non-Hermitian photon blockade was presented in the weak-coherent-coupling regime [75]. In the current scheme, we propose a method to produce non-Hermitian anharmonicity by engineering magnon-qubit purely dissipative coupling, which induces a strong non-Hermitian magnon blockade (NHMB). We find that the high magnon occupancy probability that corresponds to high efficiency of the MB and the small value of the second-order

[*]Contact author: haoxiong1217@gmail.com

correlation function (SOCF) that contributes to the high purity of the MB simultaneously occur for the NHMB, which provides an effective avenue for realizing high-efficiency and high-purity single-magnon-level quantum manipulation in non-Hermitian systems. In addition, the conventional magnon blockade (CMB) caused by the anharmonicity of energy levels is realized in the braided configuration because of the occurrence of a decoherence-free interaction between the GSE and the GA [42]. More interestingly, the CMB induced by the inhomogeneous broadening of the anharmonic energy levels [21] and the unconventional magnon blockade (UMB) stemming from the destructive interference of different paths can emerge simultaneously, which occurs in the braided and nested coupling configurations. The switching between the CMB and the UMB is completed by regulating the phase, which indicates that the efficiency and purity of a single magnon have high tunability since the CMB has a high average magnon number and UMB has a smaller SOCF value. For the separate configuration, the frequency-tunable NHMB can be obtained because of the adjustability of the Lamb shifts. Compared to previous schemes of MB [15–29], we realize the NHMB and use it to achieve a high-efficiency and high-purity single magnon. Our scheme achieves MB effects induced by four physical mechanisms and their conversion only requires modulating the phase, which shows that the GSE-GA-waveguide system provides an ideal platform for studying different MB effects and performing quantum magnon control. In particular, for the scheme that only completes the CMB effect in a magnon-qubit-waveguide system [21], the NHMB and UMB implemented in our work greatly improve the purity of the MB. In addition, the coupling configuration offers also a way of regulating the MB. Thus, we can obtain the desired single-magnon generation based on the GSE-GA-waveguide system. Our results can be applied to quantum magnon devices of different demands and on-chip magnon control.

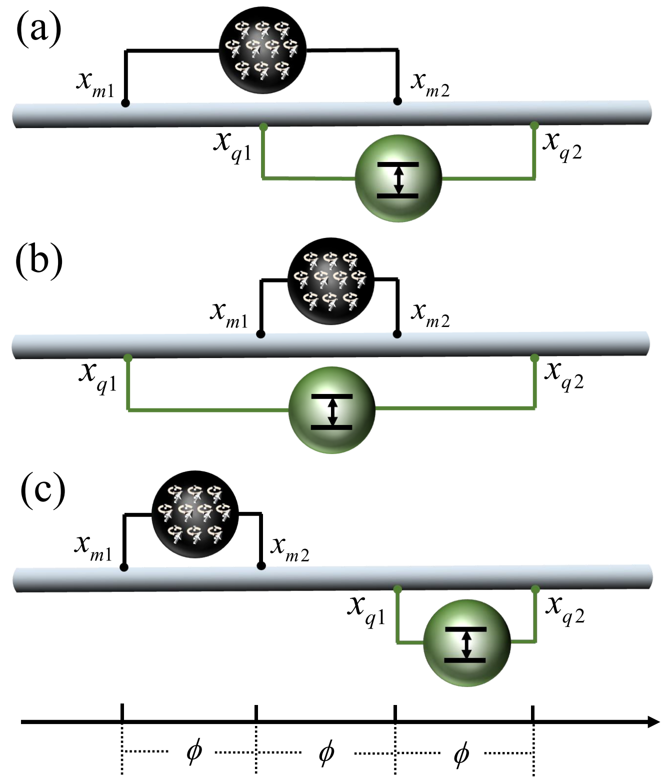

FIG. 1. Schematic diagram of the GSE-GA-waveguide QED system: (a) braided coupling configurations, (b) nested coupling configurations, and (c) separate coupling configuration. Both the GSE and the GA couple to the common waveguide at two coupling points and the distance of the neighboring coupling points is d. Here $\phi = kd$ is the accumulated phase caused by the photon with wave vector k propagating between neighboring coupling points.

II. MODEL AND EQUATIONS

As intuitively described in Fig. 1, the GSE consists of a yttrium iron garnet (YIG) sphere which supports the magnon mode and can couple to the waveguide twice. The two-level GA simultaneously couples to the common waveguide with two coupling points. They form three different coupling configurations: a braided configuration, a nested configuration, and a separate configuration. Here $\phi = kd$ is the accumulated phase of a photon propagating between neighboring coupling points, where k is the wave vector of the photon and d denotes the distance between the neighboring coupling points. The master equation of the system can be given by [42,54,55,71]

$$\begin{aligned}\dot{\rho} = & -i[H_0, \rho] + (\kappa_m + \Gamma_m)\mathcal{L}[m]\rho + (\gamma_q + \Gamma_q)\mathcal{L}[\sigma]\rho \\ & + \Gamma_c\big(m\rho\sigma^\dagger - \tfrac{1}{2}\{\sigma^\dagger m, \rho\} + \sigma\rho m^\dagger - \tfrac{1}{2}\{m^\dagger\sigma, \rho\}\big), \quad (1)\end{aligned}$$

where $\mathcal{L}[o]\rho = o\rho o^\dagger - \frac{1}{2}\{o^\dagger o, \rho\}$ is the Lindblad superoperator with $o = m, \sigma$; m ($m^\dagger$) is the annihilation (creation) operator of the magnon mode in the GSE, and σ ($\sigma^\dagger$) denotes the lowering (raising) operator of the GA; κ_m and γ_q are the intrinsic damping rates of the GSE and the GA, respectively; $H_0 = \tilde{\Delta}_m m^\dagger m + \tilde{\Delta}_q \sigma^\dagger\sigma + g_{mq}(m^\dagger\sigma + \sigma^\dagger m) + H_d$; $H_d = \xi_m(m^\dagger + m)$ is the driving term of the system; $\tilde{\Delta}_j = \Delta_j + \delta_j$ ($j = m, q$); $\Delta_j = \omega_j - \omega_d$ is the frequency detuning between the GSE or the GA frequency ω_j and the driving field ξ_m with the frequency ω_d; $\delta_j = \frac{\gamma_0}{2}\sum_{\alpha,\beta=1,2}\sin(k|x_{j\alpha} - x_{j\beta}|)$ is the Lamb shift of the GSE or the GA; $g_{mq} = \frac{\gamma_0}{2}\sum_{\alpha,\beta=1,2}\sin(k|x_{m\alpha} - x_{q\beta}|)$ represents the exchange interaction strength between the GSE and the GA; $\Gamma_j = \gamma_0\sum_{\alpha,\beta=1,2}\cos(k|x_{j\alpha} - x_{j\beta}|)$ is the individual decay rate of the GSE or the GA; and $\Gamma_c = \gamma_0\sum_{\alpha,\beta=1,2}\cos(k|x_{m\alpha} - x_{q\beta}|)$ is the collective decay term for the GSE and the GA. Here the external damping rates for both the GSE and the GA emitted to the waveguide at each coupling points are $\gamma_{0m} = \gamma_{0q} = \gamma_0$. When the system is in the steady state, the SOCF is characterized by $g^{(2)}(0) = \mathrm{Tr}(m^\dagger m^\dagger m m\rho)/[\mathrm{Tr}(m^\dagger m\rho)]^2$. Here $g^{(2)}(0) > 1$ corresponds to the magnon bunching effect. When $g^{(2)}(0) < 1$, this is the magnon antibunching effect. Further, $g^{(2)}(0) \to 0$ indicates that the perfect MB occurs. The statistical properties of the magnon can be studied by solving numerically the master equation [76].

We can also obtain the analytical expression of the SOCF by solving the Schrödinger equation $i\partial|\Psi\rangle/\partial t = H_{\mathrm{eff}}|\Psi\rangle$ in the weak-driving-field limit. The effective Hamiltonian can be written as

$$H_{\text{eff}} = \left(\tilde{\Delta}_m - \frac{i}{2}\tilde{\kappa}_m\right)m^\dagger m + \left(\tilde{\Delta}_q - \frac{i}{2}\tilde{\gamma}_q\right)\sigma^\dagger\sigma + \left(g_{mq} - \frac{i}{2}\Gamma_c\right)(m^\dagger\sigma + \sigma^\dagger m) + H_d, \quad (2)$$

in which $\tilde{\kappa}_m = \kappa_m + \Gamma_m$ and $\tilde{\gamma}_q = \gamma_q + \Gamma_q$. The wave function $|\Psi\rangle = \sum_{n=0}^{n=2} C_{n,g}|n, g\rangle + \sum_{n=0}^{n=1} C_{n,e}|n, e\rangle$, where $C_{n,\mu}$ ($\mu = g, e$) denotes the probability amplitudes of the system in the state $|n, \mu\rangle$. The equations of the probability amplitudes are

$$\begin{aligned}
i\dot{C}_{1,g} &= \left(\tilde{\Delta}_m - \frac{i}{2}\tilde{\kappa}_m\right)C_{1,g} + \left(g_{mq} - \frac{i}{2}\Gamma_c\right)C_{0,e} + \xi_m,\\
i\dot{C}_{2,g} &= 2\left(\tilde{\Delta}_m - \frac{i}{2}\tilde{\kappa}_m\right)C_{2,g} + \sqrt{2}\left(g_{mq} - \frac{i}{2}\Gamma_c\right)C_{1,e}\\
&\quad + \sqrt{2}\xi_m C_{1,g},\\
i\dot{C}_{0,e} &= \left(\tilde{\Delta}_q - \frac{i}{2}\tilde{\gamma}_q\right)C_{0,e} + \left(g_{mq} - \frac{i}{2}\Gamma_c\right)C_{1,g},\\
i\dot{C}_{1,e} &= \left(\tilde{\Delta}_m + \tilde{\Delta}_q - \frac{i}{2}(\tilde{\kappa}_m + \tilde{\gamma}_q)\right)C_{1,e}\\
&\quad + \sqrt{2}\left(g_{mq} - \frac{i}{2}\Gamma_c\right)C_{2,g} + \xi_m C_{0,e}.
\end{aligned} \quad (3)$$

The SOCF of the steady state can be approximately expressed as

$$g^{(2)}(0) \simeq \frac{2|C_{g,2}|^2}{|C_{g,1}|^4} = \frac{|\eta_1 - i\aleph_1|^2|\eta_2 - i\aleph_2|^2}{|2\tilde{\Delta}_q - i\tilde{\gamma}_q|^4|\chi|^4}, \quad (4)$$

in which $\eta_1 = 4\tilde{\Delta}_q(\tilde{\Delta}_m + \tilde{\Delta}_q) - \tilde{\gamma}_q(\tilde{\gamma}_q + \tilde{\kappa}_m) + 4g_{mq}^2 - \Gamma_c^2$, $\aleph_1 = 2\tilde{\Delta}_q(\tilde{\kappa}_m + \tilde{\gamma}_q) + 2\tilde{\gamma}_q(\tilde{\Delta}_m + \tilde{\Delta}_q) + 4g_{mq}\Gamma_c$, $\eta_2 = 4g_{mq}^2 - \Gamma_c^2 + \tilde{\kappa}_m\tilde{\gamma}_q - 4\tilde{\Delta}_m\tilde{\Delta}_q$, $\aleph_2 = 4g_{mq}\Gamma_c - 2\tilde{\Delta}_q\tilde{\kappa}_m - 2\tilde{\Delta}_m\tilde{\gamma}_q$, and $\chi = 4(g_{mq} - \frac{i}{2}\Gamma_c)^2 + (\tilde{\kappa}_m + 2i\tilde{\Delta}_m)(2i\tilde{\Delta}_m + 2i\tilde{\Delta}_q + \tilde{\kappa}_m + \tilde{\gamma}_q)$.

III. RESULTS AND DISCUSSION

We first study the properties of the MB in the braided coupling configuration [Fig. 1(a)]. In this scenario, $\delta_m = \delta_q = \gamma_0 \sin(2\phi)$, $g_{mq} = \frac{\gamma_0}{2}[3\sin\phi + \sin(3\phi)]$, $\Gamma_m = \Gamma_q = 2\gamma_0[1 + \cos(2\phi)]$, and $\Gamma_c = \gamma_0[3\cos\phi + \cos(3\phi)]$. Figure 2(a) shows the logarithmic SOCF $\log_{10}[g^{(2)}(0)]$ varying with the detuning Δ and the phase ϕ. For simplicity, we have set $\Delta_m = \Delta_q = \Delta$ and $\kappa_m = \gamma_q = \kappa$. Obviously, the statistical properties of the magnon have a strong dependence on the phase. The bunching and antibunching effects of the magnon can be periodically switched by tailoring the phase. From Figs. 2(b) and 2(c) we can see that for both the SOCF and the mean magnon number, the analytical results fit well with the numerical simulation, which verifies the credibility of our results. In order to explore the physical mechanism of MB generation in the GSE-GA-waveguide system, we can derive the energy eigenvalues in the diagram of a dressed state

$$\omega_{n,\pm} = n\tilde{\omega}'_m + \frac{1}{2}\tilde{\Delta}' \pm \frac{1}{2}\sqrt{4n\left(g_{mq} - \frac{i}{2}\Gamma_c\right)^2 + \tilde{\Delta}'^2}, \quad (5)$$

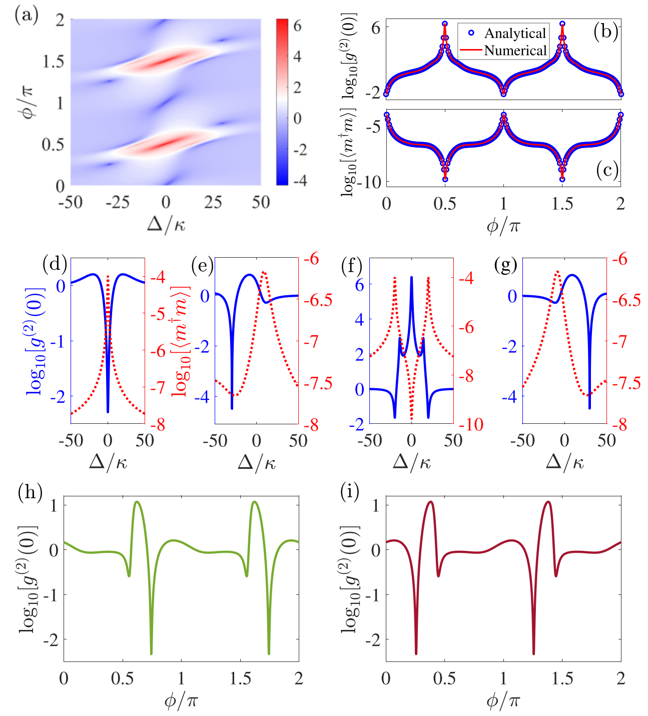

FIG. 2. Properties of the MB in the braided coupling configuration. (a) Plot of $\log_{10}[g^{(2)}(0)]$ varying with Δ and ϕ. (b) Plot of $\log_{10}[g^{(2)}(0)]$ and (c) plot of $\log_{10}[\langle m^\dagger m\rangle]$ versus ϕ when $\Delta = 0$. Also shown are plots of $\log_{10}[g^{(2)}(0)]$ and $\log_{10}[\langle m^\dagger m\rangle]$ versus Δ for (d) $\phi = 0$, (e) $\phi = 0.254\pi$, (f) $\phi = 0.5\pi$, and (g) $\phi = 0.746\pi$. In addition, $\log_{10}[g^{(2)}(0)]$ is plotted versus ϕ for (h) $\Delta = 29\kappa$ and (i) $\Delta = -29\kappa$. The other parameters are $\kappa_m = \gamma_q = \kappa$, $\gamma_0 = 20\kappa$, and $\xi_m = 0.01\kappa$.

with $\tilde{\omega}'_m = \tilde{\omega}_m - \frac{i}{2}\tilde{\kappa}_m$, $\tilde{\omega}'_q = \tilde{\omega}_q - \frac{i}{2}\tilde{\gamma}_q$, $\tilde{\Delta}' = \tilde{\omega}'_q - \tilde{\omega}'_m$, and $\tilde{\omega}_j = \omega_j + \delta_j$. The real and imaginary parts of $\omega_{n,\pm}$ denote the frequencies and dissipations of the energy levels, respectively. It is worth emphasizing that the dissipation can give rise to the extended bandwidth of the energy levels. For $\phi = 2\varsigma\pi$ (ς is an integer), $\delta_j = 0$, $g_{mq} = 0$, $\Gamma_j = 4\gamma_0$, and $\Gamma_c = 4\gamma_0$. Thus, the magnon-qubit coupling only includes the dissipative part. According to Eq. (5), in the case of $\omega_m = \omega_q = \omega$ and $\kappa_m = \gamma_q = \kappa$, we can obtain $\mathrm{Re}(\omega_{1,\pm}) = \omega$ and $\mathrm{Re}(\omega_{2,\pm}) = 2\omega$, which indicates harmonicity in the energy levels. However, the dissipations of the energy levels are anharmonic. In particular, $\mathrm{Im}(\omega_{1,-}) = \kappa/2 \ll \mathrm{Im}(\omega_{2,-}) = [2\kappa + (8 - 4\sqrt{2})\gamma_0]/2$ for $\gamma_0 \gg \kappa$. Thus, the two-magnon state can be effectively eliminated from the dynamics so that the absorption of the second magnon is prevented and the SOCF is markedly suppressed for $\Delta = 0$, as shown in Fig. 2(d). The corresponding schematic of non-Hermitian anharmonicity is sketched in Fig. 3(a). Our scheme actually implements a method for generating non-Hermitian anharmonicity based on magnon-qubit purely dissipative coupling rather than weak coherent coupling [75] and the so-called NHMB derived from the non-Hermitian anharmonicity mechanism is realized. When $\phi = (2\varsigma + 1)\pi$, $\Gamma_c = -4\gamma_0$ and the other parameters are the same as the situation for $\phi = 2\varsigma\pi$. In addition, $\mathrm{Im}(\omega_{1,+}) \ll \mathrm{Im}(\omega_{2,+})$ is obtained. So the NHMB can be achieved at $\Delta = 0$ for $\phi = \varsigma\pi$.

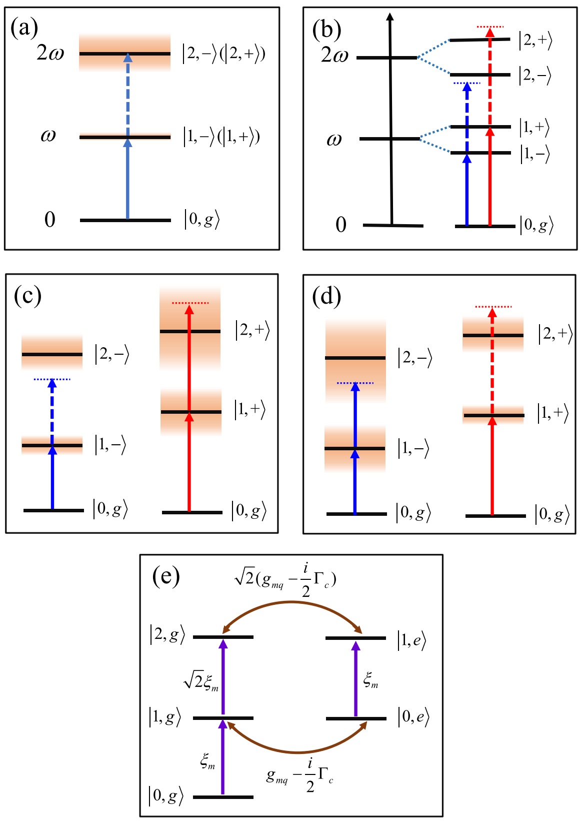

FIG. 3. (a) Schematic of non-Hermitian anharmonicity (anharmonic dissipation of the harmonic energy level) where the magnon-qubit coupling is purely dissipative. (b) Anharmonic energy-level structure during the decoherence-free interaction between the GSE and the GA, i.e., the magnon-qubit coupling only involves the coherent part. (c) and (d) Inhomogeneous broadening of the anharmonic energy levels in which both the coherent and dissipative couplings exist. (e) Transition paths for different magnon states.

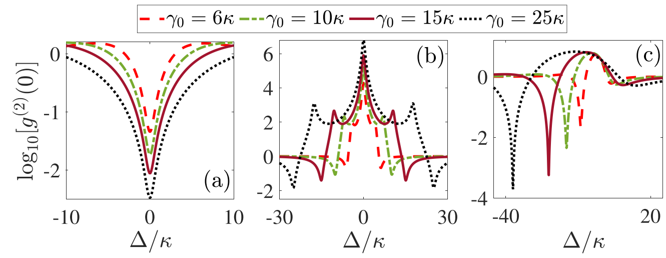

FIG. 4. Properties of the MB in the braided coupling configuration. Here $\log_{10}[g^{(2)}(0)]$ is plotted versus Δ for (a) $\phi = 0$, (b) $\phi = 0.5\pi$, and (c) $\phi = 0.254\pi$ for different values of γ_0. The other parameters are the same as in Fig. 2.

When ϕ is tuned to $(\frac{1}{2} + \varsigma)\pi$, $g_{mq} = \pm\gamma_0$ and $\delta_j = \Gamma_j = \Gamma_c = 0$. The decoherence-free interaction between the GSE and the GA is achieved [42]. In other words, purely coherent magnon-qubit coupling occurs. Two MB points located at positions $\Delta = \pm g_{mq}$ are presented in Fig. 2(f). From Fig. 3(b) we can see that the transition from the state $|0, g\rangle$ to the state $|1, \pm\rangle$ is resonant with the frequency ω_d of the driving field. However, the transition $|1, \pm\rangle \to |2, \pm\rangle$ is far from resonance. Thereby, the CMB can be caused by the anharmonic energy levels.

For the case where the coherent and dissipative couplings exist simultaneously, i.e., $\phi \neq \varsigma\pi$ and $\phi \neq (\frac{1}{2} + \varsigma)\pi$, strong MB effects can also be observed in Fig. 2(a). More clearly, two MB valleys appear simultaneously in Figs. 2(e) and 2(g) when $\phi \to \pi/4$ and $3\pi/4$, respectively. As described in Fig. 3(c), for $\phi \to \pi/4$ and the diving field frequency $\omega_d = \mathrm{Re}(\omega_{1,-})$, we can obtain $|\mathrm{Im}(\omega_{2,-})/2| < |\mathrm{Re}(\omega_{2,-}) - \mathrm{Re}(\omega_{1,-}) - \omega_d|$. Under this condition, the state $|2, -\rangle$ cannot be populated, which causes the MB to occur at $\Delta \approx g_{mq} - \delta_j = (\sqrt{2} - 1)\gamma_0$ on the basis of Eq. (5), which can also be seen in Fig. 2(e) (the right valley of the MB). Therefore, the inhomogeneous broadening of the anharmonic energy levels induces the CMB [21]. However, in the case of $\omega_d = \mathrm{Re}(\omega_{1,+})$, we can find $|\mathrm{Im}(\omega_{2,+})/2| > |\mathrm{Re}(\omega_{2,+}) - \mathrm{Re}(\omega_{1,+}) - \omega_d|$. The state $|2, +\rangle$ can be excited. The magnon statistics exhibit the bunching effect, i.e., $g^{(2)}(0) > 1$. When the phase is tuned to $\phi \to 3\pi/4$, the CMB effect can be opened for $\omega_d = \mathrm{Re}(\omega_{1,+})$ and closed for $\omega_d = \mathrm{Re}(\omega_{1,-})$, as shown in Fig. 3(d). The valley of the CMB can be located in the region of $\Delta \approx -g_{mq} - \delta_j = (1 - \sqrt{2})\gamma_0$ of Fig. 2(g) (the left valley of the MB). Meanwhile, we can obtain a stronger MB point that corresponds to the left deep dip of Fig. 2(e) or the right deep dip of Fig. 2(g). The physical mechanism results from the destructive interference of two paths, i.e., $|1, g\rangle \xrightarrow{\sqrt{2}\xi_m} |2, g\rangle$ and $|1, g\rangle \xrightarrow{g_{mq} - i\Gamma_c/2} |0, e\rangle \xrightarrow{\xi_m} |1, e\rangle \xrightarrow{\sqrt{2}(g_{mq} - i\Gamma_c/2)} |2, g\rangle$ [Fig. 3(e)], which is the UMB. The coexistence phenomenon of the CMB and UMB emerges and this can be extended to the condition of $\phi \to (\frac{1}{4} + \varsigma/2)\pi$. When ϕ is away from $(\frac{1}{4} + \varsigma/2)\pi$, the UMB vanishes and only the CMB induced by the inhomogeneous broadening of the anharmonic energy levels appears at $\Delta \approx g_{mq} - \delta_j$ or $\Delta \approx -g_{mq} - \delta_j$. As can be seen in Figs. 2(h) and 2(i), for a certain frequency, the switching between the CMB and the UMB can be fulfilled by tuning the phase. Thereby, the phase can be viewed as a switch to periodically convert the efficiency (highly coherent excitation of the magnon) and purity (small value of the SOCF) of producing a single magnon since the CMB has a relatively high magnon number and the UMB has a smaller SOCF value, which can be verified in Figs. 2(e)–2(g). In addition, we study the influence of γ_0 on the MB. It can be observed in Fig. 4 that MB effects can still occur even for small γ_0. The purity and optimal frequency point of the MB can be modulated, whether a NHMB, CMB, or UMB, via γ_0. Based on the above analysis, we use the phase to simultaneously modulate the Lamb shift δ_j, the individual decay rate Γ_j, the exchange interaction strength (magnon-qubit coherent coupling strength) g_{mq}, and the collective decay term (twice the magnon-qubit dissipative coupling strength) Γ_c and further achieve the conversion of MB effects induced by four different mechanisms. Thereby, our scheme opens a path for implementing and flexibly modulating magnon-qubit coupling [6,9,77]. Herein, MB effects induced by four physical mechanisms have been achieved by a single physical system [Figs. 3(a)–3(e)]. Therefore, the GSE-GA-waveguide system shows unique advantages over previous schemes of the MB [15–29] in realizing a single magnon and quantum control. Our proposal demonstrates that extending the magnon-qubit

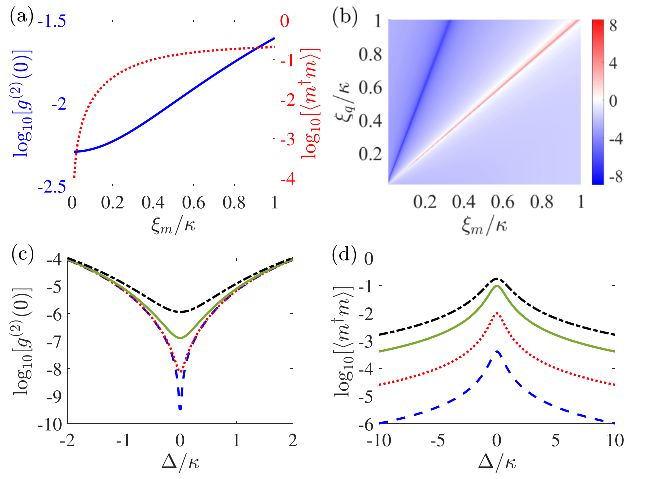

FIG. 5. Properties of the NHMB versus the driving fields. (a) Plot of $\log_{10}[g^{(2)}(0)]$ and $\log_{10}[\langle m^\dagger m\rangle]$ versus ξ_m for $\phi = 0$ and $\Delta = 0$ for the case of a single field ξ_m. (b) Plot of $\log_{10}[g^{(2)}(0)]$ varying with the driving fields ξ_m and ξ_q for $\phi = 0$ and $\Delta = 0$. (c) Plot of $\log_{10}[g^{(2)}(0)]$ and (d) plot of $\log_{10}[\langle m^\dagger m\rangle]$ versus Δ for the case of two fields for $\xi_m = 0.01\kappa$ and $\xi_q = 0.0305\kappa$ (blue dashed line), $\xi_m = 0.05\kappa$ and $\xi_q = 0.1527\kappa$ (red dotted line), $\xi_m = 0.2\kappa$ and $\xi_q = 0.61\kappa$ (green solid line), and $\xi_m = 0.4\kappa$ and $\xi_q = 1.22\kappa$ (black dash-dotted line). The other parameters are the same as in Fig. 2.

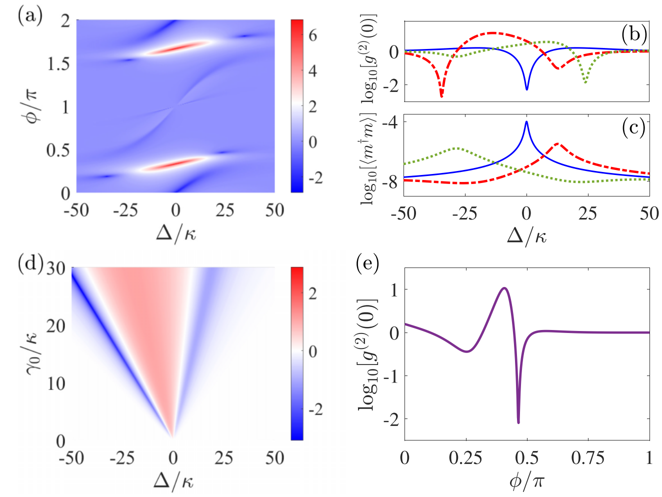

FIG. 6. Properties of the MB in the nested coupling configuration. (a) Plot of $\log_{10}[g^{(2)}(0)]$ varying with Δ and ϕ. (b) Plot of $\log_{10}[g^{(2)}(0)]$ and (c) plot of $\log_{10}[\langle m^\dagger m\rangle]$ versus Δ for $\phi = 0$ (blue solid line), $\phi = 0.187\pi$ (red dash-dotted line), and $\phi = 0.468\pi$ (green dotted line). (d) Plot of $\log_{10}[g^{(2)}(0)]$ varying with Δ and γ_0 for $\phi = 0.187\pi$. (e) Plot of $\log_{10}[g^{(2)}(0)]$ versus ϕ for $\Delta = 23\kappa$. The other parameters are the same as in Fig. 2.

waveguide with single-point coupling [21] to the GSE-GA-waveguide system not only contributes to the study of MB effects by more physical mechanisms, but also improves the purity of single-magnon generation through implementations of the NHMB and UMB. Our scheme provides an ideal platform for studying the MB with multiple physical mechanisms and producing a single-magnon source on demand.

From the perspective of producing a high-quality single-magnon source, we can see that the NHMB has both high magnon number excitation and a low SOCF [Fig. 2(d)], which are high-efficiency and high-purity MB effects [34–36]. In Fig. 5(a) we plot $\log_{10}[g^{(2)}(0)]$ and $\log_{10}[\langle m^\dagger m\rangle]$ versus ξ_m. By regulating ξ_m, we can obtain a higher magnon occupancy probability while keeping the small value of the SOCF. In particular, $g^{(2)}(0) \sim 0.01$ and $\langle m^\dagger m\rangle \sim 0.1$ when $\xi_m = 0.5\kappa$. To further explore and improve the efficiency and purity of the NHMB, we added an additional driving field ξ_q to drive the GA. The driving term can be rewritten as $H_d = \xi_m(m^\dagger + m) + \xi_q(\sigma^\dagger + \sigma)$ in Eqs. (1) and (2). The purity of the NHMB varying with ξ_m and ξ_q is shown in Fig. 5(b). It can be observed that the optimal purity of the NHMB occurs under the condition $\xi_q \sim 3\xi_m$. In particular, the SOCF $g^{(2)}(0) \sim 10^{-9.5}$ and $\langle m^\dagger m\rangle \sim 10^{-4}$ are obtained from Figs. 5(c) and 5(d), which confirms that the purity of the NHMB can be improved by seven orders of magnitude compared to Fig. 2(d) while maintaining the same efficiency by introducing the driving field of the GA. Compared to previous schemes of the MB [15–29], the completion of the NHMB in our work can greatly improve the purity of single-magnon generation. In particular, we improve the purity of the MB by about eight orders of magnitude relative to the magnon-qubit system coupled to a waveguide with single-point coupling [21]. Furthermore, by modulating the driving fields, $g^{(2)}(0) \sim 10^{-7}$ and $\langle m^\dagger m\rangle \sim 0.1$, and $g^{(2)}(0) \sim 10^{-6}$ and $\langle m^\dagger m\rangle \sim 0.2$ are achieved. Thus, the GSE-GA system coupled to a waveguide can be applied to prepare a high-efficiency and high-purity single-magnon source with high tunability.

For the nested coupling configuration [Fig. 1(b)], $\delta_m = \gamma_0 \sin\phi$, $\delta_q = \gamma_0 \sin(3\phi)$, $g_{mq} = \gamma_0[\sin\phi + \sin(2\phi)]$, $\Gamma_m = 2\gamma_0(1 + \cos\phi)$, $\Gamma_q = 2\gamma_0[1 + \cos(3\phi)]$, and $\Gamma_c = 2\gamma_0[\cos\phi + \cos(2\phi)]$. The NHMB can still be realized at $\Delta = 0$ when $\phi = 2\varsigma\pi$, as shown in Fig. 6(a). However, for $\phi = (2\varsigma + 1)\pi$, $\delta_j = g_{mq} = \Gamma_j = \Gamma_c = 0$, which means that the GSE and the GA are decoupled and so the MB vanishes. The coexistence phenomenon of the CMB and the UMB can be found from Figs. 6(b) and 6(c), where the higher-purity CMB is fulfilled compared to the braided coupling configuration. In addition, the purity and the frequency width of generating the CMB and UMB can be enhanced simultaneously when γ_0 is increased [Fig. 6(d)]. We can also obtain the MB or the single magnon of the required frequency based on the adjustment of γ_0. By regulating the phase, the magnon antibunching can also be modulated from the CMB to the UMB, as in Fig. 6(e).

In the case of the separate coupling configuration depicted in Fig. 1(c), $\delta_m = \delta_q = \gamma_0 \sin\phi$, $g_{mq} = \frac{\gamma_0}{2}[\sin\phi + 2\sin(2\phi) + \sin(3\phi)]$, $\Gamma_m = \Gamma_q = 2\gamma_0(1 + \cos\phi)$, and $\Gamma_c = \gamma_0[\cos\phi + 2\cos(2\phi) + \cos(3\phi)]$. From Figs. 7(a) and 7(b) it can be seen that the NHMB occurs not only in $\phi = 2\varsigma\pi$ but also in $\phi = (\frac{1}{2} + \varsigma)\pi$. This is because only dissipative coupling exists between the GSE and the GA, i.e., $g_{mq} = 0$ and $\Gamma_c = -2\gamma_0$ for $\phi = (\frac{1}{2} + \varsigma)\pi$ and $\delta_j = \gamma_0$ ($\delta_j = -\gamma_0$) when $\phi = (\frac{1}{2} + 2\varsigma)\pi$ [$\phi = (\frac{3}{2} + 2\varsigma)\pi$]. The optimal frequency point of the NHMB deviates from the resonance point and appears at $\Delta = \pm\gamma_0$. Thus, the frequency of producing the NHMB can be adjusted flexibly by γ_0 [Fig. 7(c)], which extends the frequency tunability of the NHMB compared to the braided and nested coupling configurations and the

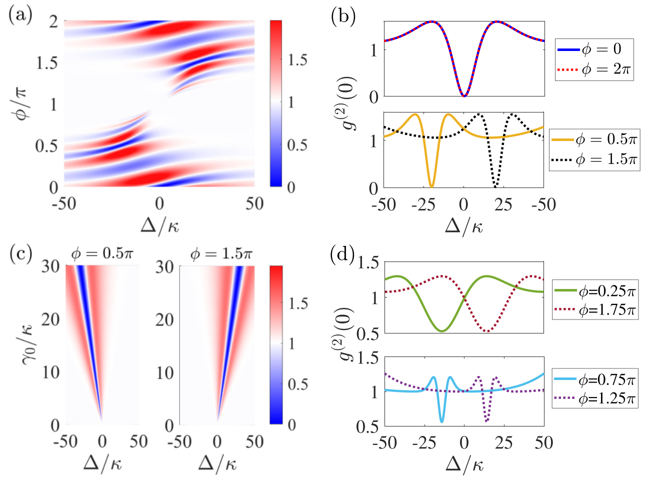

FIG. 7. Properties of the MB in the separate coupling configuration. (a) Plot of $g^{(2)}(0)$ varying with Δ and ϕ. (b) and (d) Plot of $g^{(2)}(0)$ versus Δ for different values of ϕ. (c) Plot of $g^{(2)}(0)$ varying with Δ and γ_0 for $\phi = 0.5\pi$ or 1.5π. The other parameters are the same as in Fig. 2.

previous non-Hermitian blockade scheme [75]. In addition, from Fig, 7(d) we can also see the UMB for the phase $\phi = (\frac{1}{4} + \varsigma/2)\pi$. However, the CMB and the UMB cannot emerge synchronously in the separate coupling configuration. This demonstrates that different coupling configurations have their own advantages in accomplishing the MB, which means that the coupling configuration can offer another degree of freedom for the regulation of the MB in our scheme and can serve as an innovative quantum control tool in the research field of the MB [15–29]. Therefore, we can obtain the desired single magnon by changing coupling configurations.

In a real situation, the intrinsic damping rates κ_m and γ_q and external damping rates γ_{0q} and γ_{0m} can be modulated and are different, which provides an efficient way to realize quantum magnon control. For the case of $\gamma_{0m} \neq \gamma_{0q}$, we obtain $\delta_m = \gamma_{0m}\sin(2\phi)$, $\delta_q = \gamma_{0q}\sin(2\phi)$, $g_{mq} = \frac{\sqrt{\gamma_{0m}\gamma_{0q}}}{2}[3\sin\phi + \sin(3\phi)]$, $\Gamma_m = 2\gamma_{0m}[1+\cos(2\phi)]$, $\Gamma_q = 2\gamma_{0q}[1+\cos(2\phi)]$, and $\Gamma_c = \sqrt{\gamma_{0m}\gamma_{0q}}[3\cos\phi + \cos(3\phi)]$ in the braided coupling configuration. For the nested coupling configuration, $\delta_m = \gamma_{0m}\sin\phi$, $\delta_q = \gamma_{0q}\sin(3\phi)$, $g_{mq} = \sqrt{\gamma_{0m}\gamma_{0q}}[\sin\phi + \sin(2\phi)]$, $\Gamma_m = 2\gamma_{0m}[1+\cos\phi]$, $\Gamma_q = 2\gamma_{0q}[1+\cos(3\phi)]$, and $\Gamma_c = 2\sqrt{\gamma_{0m}\gamma_{0q}}[\cos\phi + \cos(2\phi)]$. The physical quantities in the scenario of separate coupling are expressed as $\delta_m = \gamma_{0m}\sin\phi$, $\delta_q = \gamma_{0q}\sin\phi$, $g_{mq} = \frac{\sqrt{\gamma_{0m}\gamma_{0q}}}{2}[\sin\phi + 2\sin(2\phi) + \sin(3\phi)]$, $\Gamma_m = 2\gamma_{0m}(1+\cos\phi)$, $\Gamma_q = 2\gamma_{0q}(1+\cos\phi)$, and $\Gamma_c = \sqrt{\gamma_{0m}\gamma_{0q}}[\cos\phi + 2\cos(2\phi) + \cos(3\phi)]$. We show in Fig. 8 the influence of different intrinsic and external damping rates of the GSE and GA on the MB effect and we have selected experimentally feasible parameters in the numerical simulations based on a recent experiment on giant superconducting qubits coupled to the superconducting microwave coplanar waveguide (CPW) and YIG spheres coupled to the superconducting microwave CPW [57,65]. To simplify and distinguish the NHMB with an adjustable frequency of the separate coupling configuration, the NHMB

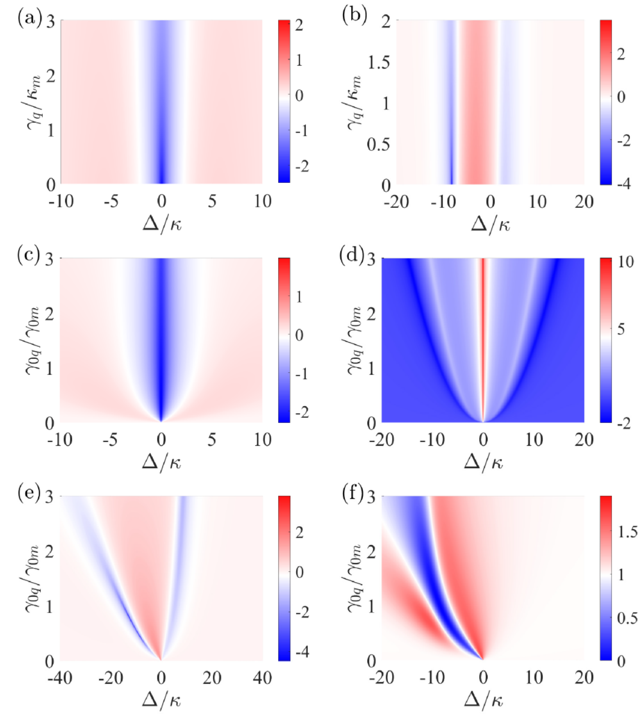

FIG. 8. Plot of $\log_{10}[g^{(2)}(0)]$ varying with Δ and γ_q/κ_m for (a) $\phi = 0$ in all three coupling configurations and (b) $\phi = 0.1855\pi$ in the nested coupling configuration when $\gamma_{0q} = 3.68\kappa = 2\pi \times 3.68$ MHz [57]. Plot of $\log_{10}[g^{(2)}(0)]$ varying with Δ and γ_{0q}/γ_{0m} for (c) $\phi = 0$ in all three coupling configurations, (d) $\phi = 0.5\pi$ in the braided coupling configuration, and (e) $\phi = 0.1855\pi$ in the nested coupling configuration. (f) Plot of $g^{(2)}(0)$ varying with Δ and γ_{0q}/γ_{0m} for $\phi = 0.5\pi$ in the separate coupling configuration. In (c)–(f) $\gamma_q = 0.03\kappa = 2\pi \times 0.03$ MHz [57]. The other parameters are [65] $\kappa_m = \kappa = 2\pi \times 1$ MHz, $\gamma_{0m} = 8.5\kappa = 2\pi \times 8.5$ MHz, and the same as in Fig. 2.

that can be realized in all three coupling configurations for $\phi = 2\varsigma\pi$, we call this MB a resonance NHMB (RNHMB) because it only occurs at $\Delta = 0$. Figures 8(a) and 8(b) show the RNHMB and coexisting CMB and UMB of the nested coupling configuration varying with the ratio γ_q/κ_m of intrinsic damping rates. It can be seen that the ratio of intrinsic damping rates has a small effect on the MB produced by each physical mechanism. Therefore, the purity of the MB of our scheme is robust to intrinsic damping rates. Furthermore, for the ratio γ_{0q}/γ_{0m} of external damping rates, it can hardly change the properties of the RNHMB, as shown in Fig. 8(c). However, γ_{0q}/γ_{0m} can regulate flexibly optimal frequency points and the purity of the CMB of the braided coupling configuration, the coexisting CMB and UMB of the nested coupling configuration, and the Lamb-shift-induced frequency-tunable NHMB of the separate coupling configuration [Figs. 8(d)–8(f)]. In order to more clearly exhibit the MB properties in the case of $\gamma_{0q} \neq \gamma_{0m}$ and $\gamma_q \neq \kappa_m$, five main MBs in different coupling configurations are shown in Figs. 9(a)–9(e). It can be observed that the purity of a single magnon is basically consistent with the situations of $\gamma_{0q} = \gamma_{0m} = \gamma_0$ and $\gamma_q = \kappa_m = \kappa$. In particular, the purity of the UMB of the nested coupling configuration

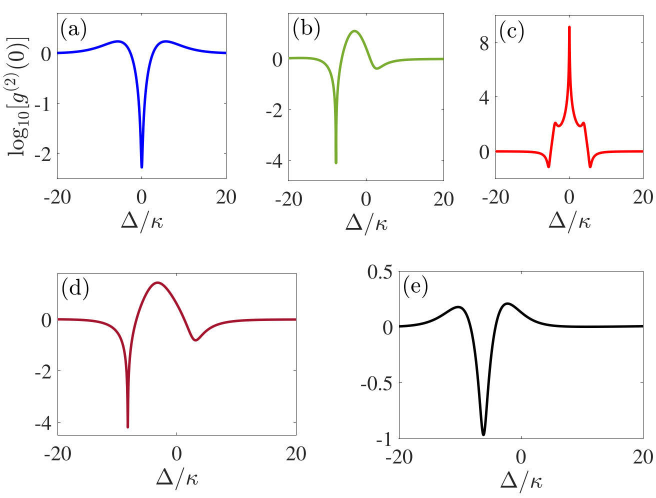

FIG. 9. Plot of $\log_{10}[g^{(2)}(0)]$ versus Δ for (a) $\phi = 0$, (b) $\phi = 0.235\pi$, and (c) $\phi = 0.5\pi$ in the braided coupling configuration, (d) $\phi = 0.1855\pi$ in the nested coupling configuration, and (e) $\phi = 0.5\pi$ in the separate coupling configuration. The other parameters are [57,65] $\kappa_m = \kappa = 2\pi \times 1$ MHz, $\gamma_q = 0.03\kappa = 2\pi \times 0.03$ MHz, $\gamma_{0m} = 8.5\kappa = 2\pi \times 8.5$ MHz, $\gamma_{0q} = 3.68\kappa = 2\pi \times 3.68$ MHz, and the same as in Fig. 2.

in Fig. 9(d) can reach 10^{-4}, which is significantly improved compared to Fig. 6. These results show that, on the one hand, the ratios of damping rates can be used as a way of regulating single-magnon generation and, on the other hand, the system parameters to generate the MB are relaxed, which is helpful in the operation and implementation of the experiment.

Here we discuss a possible experimental setup of the GSE-GA-waveguide system. In the experiment, the GSE has been demonstrated through coupling the YIG sphere to a meandering microwave waveguide at two locations [71]. The GA has been construed experimentally where a superconducting artificial qubit can couple to a meandering superconducting microwave CPW with multiple interaction points [57–59]. Recently, devoted to the development of chip-embedded hybrid magnonic circuits, the strong interaction between a YIG ferromagnetic material and a superconducting quantum circuit has been realized [65,78–83]. In particular, it was demonstrated that the magnon mode of the YIG sphere can couple to the propagating photon of the superconducting microwave CPW with a high magnon external damping rate [65]. These advanced achievements can support the experimental implementation of the GSE-GA-waveguide system through coupling the YIG sphere and superconducting qubit to the common meandering superconducting microwave CPW with multiple coupling points. The external damping rate $\gamma_{0m}/2\pi = 8.5$ MHz of the magnon mode emitted into the microwave waveguide is realized [65]. The intrinsic damping rate $\kappa_m/2\pi$ of the magnon mode in the YIG sphere is usually 1 MHz or even smaller, such as 0.5 and 0.24 MHz [3,4,66,84–86]. By further suppressing the impurity magnon and other scattering, a lower intrinsic damping rate of the magnon mode, $\kappa_m/2\pi \sim 0.1$ MHz, is expected for high-quality YIG spheres [62,87]. For a superconducting artificial qubit, an external damping rate $\gamma_{0q}/2\pi$ with the CPW can reach tens of megahertz [58,59], even about 100 MHz [88–90], and the intrinsic damping rate $\gamma_q/2\pi$ can be 0.01–1 MHz [57,90–92]. Therefore, the system parameters of our scheme are feasible based on the recent experiments. The phase caused by a photon propagating between neighboring coupling points is written as $\phi = kd = 2\pi d/\lambda$, in which the wavelength $\lambda = 2\pi v/\omega$ for waveguide modes at the GSE or GA frequency $\omega = \omega_j$ [57,71]. The phase ϕ depends on the distance between the coupling points, on the one hand, and the GSE or GA resonance frequency, on the other. The frequency of the magnon mode in the GSE is linearly proportional to the external magnetic field H, $\omega_m = \varrho H$, where $\varrho/2\pi = 28$ GHz/T is the gyromagnetic ratio [71]. The variation of the superconducting qubit frequency can be completed by applying a magnetic field [91,92]. In the experiment, the external magnetic field can be a simple and flexible way to change the phase ϕ and further to modulate MB properties.

IV. CONCLUSION

We have demonstrated a feasible scheme for realizing multiple physical mechanisms producing MBs, including the NHMB, CMB, and UMB. The MB can be switched periodically by adjusting the phase in braided, nested, and separate coupling configurations. The NHMB stemming from non-Hermitian anharmonicity can emerge in all three configurations and can be applied to produce a high-efficiency and high-purity single-magnon source. In particular, in the braided coupling configuration, the decoherence-free interaction between the GSE and the GA can be implemented so that the CMB emerges. Meanwhile, we find the coexistence phenomenon of the CMB and the UMB in the braided and nested coupling configurations and their switching is realized by modifying the phase. This achieves the highly tunable efficiency and purity of a single magnon. For the separate coupling configuration, the NHMB of tunable frequency can be obtained since non-Hermitian anharmonicity can occur for different phase values and the Lamb shifts cause the optimal point of the NHMB to shift. Thereby, the MB can be generated on demand by tuning the phase and the coupling configurations. Our scheme suggests a potential strategy for creating and controlling a single magnon based on the GSE-GA-waveguide system, which may provide new insight into the combination of the emerging quantum magnon field and GA physics, with important applications in the construction of an integrated quantum magnon network.

ACKNOWLEDGMENTS

The work was supported by the National Key Research and Development Program of China (Grant No. 2021YFA1400700), the National Natural Science Foundation of China (Grants No. 12022507 and No. 11774113), and the Fundamental Research Funds for the Central Universities (Grant No. 2019kfyRCPY111). Computations were completed on the HPC Platform of Huazhong University of Science and Technology.

[1] H. Y. Yuan, Y. Cao, A. Kamra, R. A. Duine, and P. Yan, Quantum magnonics: When magnon spintronics meets quantum information science, Phys. Rep. **965**, 1 (2022).
[2] B. Z. Rameshti, S. V. Kusminskiy, J. A. Haigh, K. Usami, D. Lachance-Quirion, Y. Nakamura, C. M. Hu, H. X. Tang, G. E. W. Bauer, and Y. M. Blanter, Cavity magnonics, Phys. Rep. **979**, 1 (2022).
[3] Y. Tabuchi, S. Ishino, T. Ishikawa, R. Yamazaki, K. Usami, and Y. Nakamura, Hybridizing ferromagnetic magnons and microwave photons in the quantum limit, Phys. Rev. Lett. **113**, 083603 (2014).
[4] X. Zhang, C.-L. Zou, L. Jiang, and H. X. Tang, Cavity magnomechanics, Sci. Adv. **2**, e1501286 (2016).
[5] J. T. Hou and L. Liu, Strong coupling between microwave photons and nanomagnet magnons, Phys. Rev. Lett. **123**, 107702 (2019).
[6] D. Lachance-Quirion, S. P. Wolski, Y. Tabuchi, S. Kono, K. Usami, and Y. Nakamura, Entanglement-based single-shot detection of a single magnon with a superconducting qubit, Science **367**, 425 (2020).
[7] Z. Shen, G.-T. Xu, M. Zhang, Y.-L. Zhang, Y. Wang, C.-Z. Chai, C.-L. Zou, G.-C. Guo, and C.-H. Dong, Coherent coupling between phonons, magnons, and photons, Phys. Rev. Lett. **129**, 243601 (2022).
[8] X.-L. Hei, P.-B. Li, X.-F. Pan, and F. Nori, Enhanced tripartite interactions in spin-magnon-mechanical hybrid systems, Phys. Rev. Lett. **130**, 073602 (2023).
[9] D. Xu, X.-K. Gu, H.-K. Li, Y.-C. Weng, Y.-P. Wang, J. Li, H. Wang, S.-Y. Zhu, and J. Q. You, Quantum control of a single magnon in a macroscopic spin system, Phys. Rev. Lett. **130**, 193603 (2023).
[10] J. Li, S. Y. Zhu, and G. S. Agarwal, Magnon-photon-phonon entanglement in cavity magnomechanics, Phys. Rev. Lett. **121**, 203601 (2018).
[11] T.-X. Lu, H. Zhang, Q. Zhang, and H. Jing, Exceptional-point-engineered cavity magnomechanics, Phys. Rev. A **103**, 063708 (2021).
[12] X. Wang, K.-W. Huang, and H. Xiong, Nonreciprocal sideband responses in a spinning microwave magnomechanical system, Opt. Express **31**, 5492 (2023).
[13] H. Xiong, Magnonic frequency combs based on the resonantly enhanced magnetostrictive effect, Fund. Res. **3**, 8 (2023).
[14] X. Zuo, Z.-Y. Fan, H. Qian, M.-S. Ding, H. Tan, H. Xiong, and J. Li, Cavity magnomechanics: From classical to quantum, New J. Phys. **26**, 031201 (2024).
[15] Z.-X. Liu, H. Xiong, and Y. Wu, Magnon blockade in a hybrid ferromagnet-superconductor quantum system, Phys. Rev. B **100**, 134421 (2019).
[16] J.-k. Xie, S.-l. Ma, and F.-l. Li, Quantum-interference-enhanced magnon blockade in an yttrium-iron-garnet sphere coupled to superconducting circuits, Phys. Rev. A **101**, 042331 (2020).
[17] C. Zhao, X. Li, S. Chao, R. Peng, C. Li, and L. Zhou, Simultaneous blockade of a photon, phonon, and magnon induced by a two-level atom, Phys. Rev. A **101**, 063838 (2020).
[18] Y. Xu, T. Yang, L. Lin, and J. Song, Conventional and unconventional magnon blockades in a qubit-magnon hybrid quantum system, J. Opt. Soc. Am. B **38**, 876 (2021).
[19] K. Wu, W.-x. Zhong, G.-l. Cheng, and A.-x. Chen, Phase-controlled multimagnon blockade and magnon-induced tunneling in a hybrid superconducting system, Phys. Rev. A **103**, 052411 (2021).
[20] X. Li, X. Wang, Z. Wu, W.-X. Yang, and A. Chen, Tunable magnon antibunching in a hybrid ferromagnet-superconductor system with two qubits, Phys. Rev. B **104**, 224434 (2021).
[21] Y. Wang, W. Xiong, Z. Xu, G.-Q. Zhang, and J.-Q. You, Dissipation-induced nonreciprocal magnon blockade in a magnon-based hybrid system, Sci. China Phys. Mech. Astron. **65**, 260314 (2022).
[22] F. Wang, C. Gou, J. Xu, and C. Gong, Hybrid magnon-atom entanglement and magnon blockade via quantum interference, Phys. Rev. A **106**, 013705 (2022).
[23] Z. Jin and J. Jing, Magnon blockade in magnon-qubit systems, Phys. Rev. A **108**, 053702 (2023).
[24] Y. Fan, J. Li, and Y. Wu, Nonclassical magnon pair generation and Cauchy-Schwarz inequality violation, Phys. Rev. A **108**, 053715 (2023).
[25] M. S. Kheirabady, E. Ghasemian, and M. K. Tavassoly, Magnon blockade and magnon-atom entanglement induced by a qutrit coupled to a ferromagnetic YIG sphere, Ann. Phys. (Berlin) **535**, 2300024 (2023).
[26] Z.-H. Yuan, Y.-J. Chen, J.-X. Han, J.-L. Wu, W.-Q. Li, Y. Xia, Y.-Y. Jiang, and J. Song, Periodic photon-magnon blockade in an optomagnonic system with chiral exceptional points, Phys. Rev. B **108**, 134409 (2023).
[27] K.-W. Huang, X. Wang, Q.-Y. Qiu, and H. Xiong, Nonreciprocal magnon blockade via the Barnett effect, Opt. Lett. **49**, 758 (2024).
[28] W. Zhang, S. Liu, S. Zhang, and H.-F. Wang, Magnon blockade induced by parametric amplification, Phys. Rev. A **109**, 043712 (2024).
[29] Y.-T. Yan, C. Zhao, D.-W. Wang, J. Yang, and L. Zhou, Simultaneous blockade of two remote magnons induced by an atom, Phys. Rev. A **109**, 023710 (2024).
[30] K. M. Birnbaum, A. Boca, R. Miller, A. D. Boozer, T. E. Northup and H. J. Kimble, Photon blockade in an optical cavity with one trapped atom, Nature (London) **436**, 87 (2005).
[31] R. Huang, A. Miranowicz, J.-Q. Liao, F. Nori, and H. Jing, Nonreciprocal photon blockade, Phys. Rev. Lett. **121**, 153601 (2018).
[32] H. Z. Shen, Y. H. Zhou, and X. X. Yi, Tunable photon blockade in coupled semiconductor cavities, Phys. Rev. A **91**, 063808 (2015).
[33] H. Flayac and V. Savona, Unconventional photon blockade, Phys. Rev. A **96**, 053810 (2017).
[34] D. Y. Wang, C. H. Bai, X. Han, S. Liu, S. Zhang, and H. F. Wang, Enhanced photon blockade in an optomechanical system with parametric amplification, Opt. Lett. **45**, 2604 (2020).
[35] C. J. Zhu, K. Hou, Y. P. Yang, and L. Deng, Hybrid level anharmonicity and interference-induced photon blockade in a two-qubit cavity QED system with dipole-dipole interaction, Photon. Res. **9**, 1264 (2021).
[36] Y.-W. Lu, J.-F. Liu, R. Li, Y. Wu, H. Tan, and Y. Li, Single-photon blockade in quasichiral atom-photon interaction: simultaneous high purity and high efficiency, New J. Phys. **24**, 053029 (2022).
[37] Z.-G. Lu, C. Shang, Y. Wu, and X.-Y. Lü, Analytical approach to higher-order correlation functions in

U(1) symmetric systems, Phys. Rev. A **108**, 053703 (2023).

[38] Z. Wu, J. Li, and Y. Wu, Phase-engineered photon correlations in weakly coupled nanofiber cavity QED, Phys. Rev. A **109**, 033709 (2024).

[39] X.-W. Xu, A.-X. Chen, and Y.-x. Liu, Phonon blockade in a nanomechanical resonator resonantly coupled to a qubit, Phys. Rev. A **94**, 063853 (2016).

[40] H. Xie, C. G. Liao, X. Shang, M. Y. Ye, and X. M. Lin, Phonon blockade in a quadratically coupled optomechanical system, Phys. Rev. A **96**, 013861 (2017).

[41] A. F. Kockum, P. Delsing, and G. Johansson, Designing frequency-dependent relaxation rates and Lamb shifts for a giant artificial atom, Phys. Rev. A **90**, 013837 (2014).

[42] A. F. Kockum, G. Johansson, and F. Nori, Decoherence-free interaction between giant atoms in waveguide quantum electrodynamics, Phys. Rev. Lett. **120**, 140404 (2018).

[43] A. Carollo, D. Cilluffo, and F. Ciccarello, Mechanism of decoherence-free coupling between giant atoms, Phys. Rev. Res. **2**, 043184 (2020).

[44] Q.-Y. Qiu, Y. Wu, and X.-Y. Lü, Collective radiance of giant atoms in non-Markovian regime, Sci. China Phys. Mech. Astron. **66**, 224212 (2023).

[45] L. Guo, A. F. Kockum, F. Marquardt, and G. Johansson, Oscillating bound states for a giant atom, Phys. Rev. Res. **2**, 043014 (2020).

[46] X. Wang, T. Liu, A. F. Kockum, H. R. Li, and F. Nori, Tunable chiral bound states with giant atoms, Phys. Rev. Lett. **126**, 043602 (2021).

[47] H. Xiao, L. Wang, Z. H. Li, X. Chen, and L. Yuan, Bound state in a giant atom-modulated resonators system, npj Quantum Inf. **8**, 80 (2022).

[48] W. Zhao and Z. Wang, Single-photon scattering and bound states in an atom-waveguide system with two or multiple coupling points, Phys. Rev. A **101**, 053855 (2020).

[49] Q. Y. Cai and W. Z. Jia, Coherent single-photon scattering spectra for a giant-atom waveguide-QED system beyond the dipole approximation, Phys. Rev. A **104**, 033710 (2021).

[50] X.-L. Yin, Y.-H. Liu, J.-F. Huang, and J.-Q. Liao, Single-photon scattering in a giant-molecule waveguide-QED system, Phys. Rev. A **106**, 013715 (2022).

[51] Y.-T. Chen, L. Du, L. Guo, Z. Wang, Y. Zhang, Y. Li, and J.-H. Wu, Nonreciprocal and chiral single-photon scattering for giant atoms, Commun. Phys. **5**, 215 (2022).

[52] G. Cai, Y. Lu, X.-S. Ma, M.-T. Cheng, and X. Huang, Frequency tunable single photon diode based on giant atom coupling to a waveguide, Opt. Express **31**, 33015 (2023).

[53] W. Gu, H. Huang, Z. Yi, L. Chen, L. Sun, and H. Tan, Correlated two-photon scattering in a one-dimensional waveguide coupled to two- or three-level giant atoms, Phys. Rev. A **108**, 053718 (2023).

[54] A. C. Santos and R. Bachelard, Generation of maximally entangled long-lived states with giant atoms in a waveguide, Phys. Rev. Lett. **130**, 053601 (2023).

[55] X.-L. Yin and J.-Q. Liao, Generation of two-giant-atom entanglement in waveguide-QED systems, Phys. Rev. A **108**, 023728 (2023).

[56] G. Andersson, B. Suri, L. Guo, T. Aref, and P. Delsing, Nonexponential decay of a giant artificial atom, Nat. Phys. **15**, 1123 (2019).

[57] B. Kannan, M. J. Ruckriegel, D. L. Campbell, A. F. Kockum, J. Braumüller, D. K. Kim, M. Kjaergaard, P. Krantz, A. Melville, B. M. Niedzielski, A. Vepsäläinen, R. Winik, J. L. Yoder, F. Nori, T. P. Orlando, S. Gustavsson, and W. D. Oliver, Waveguide quantum electrodynamics with superconducting artificial giant atoms, Nature (London) **583**, 775 (2020).

[58] A. M. Vadiraj, A. Ask, T. G. McConkey, I. Nsanzineza, C. W. S. Chang, A. F. Kockum, and C. M. Wilson, Engineering the level structure of a giant artificial atom in waveguide quantum electrodynamics, Phys. Rev. A **103**, 023710 (2021).

[59] C. Joshi, F. Yang, and M. Mirhosseini, Resonance fluorescence of a chiral artificial atom, Phys. Rev. X **13**, 021039 (2023).

[60] A. González-Tudela, C. S. Muñoz, and J. I. Cirac, Engineering and harnessing giant atoms in high-dimensional baths: A proposal for implementation with cold atoms, Phys. Rev. Lett. **122**, 203603 (2019).

[61] L. Du, Y. Zhang, J.-H. Wu, A. F. Kockum, and Y. Li, Giant atoms in a synthetic frequency dimension, Phys. Rev. Lett. **128**, 223602 (2022).

[62] F.-X. Sun, S.-S. Zheng, Y. Xiao, Q. Gong, Q. He, and K. Xia, Remote generation of magnon Schrödinger cat state via magnon-photon entanglement, Phys. Rev. Lett. **127**, 087203 (2021).

[63] W.-J. Wu, Y.-P. Wang, J.-Z. Wu, J. Li, and J. Q. You, Remote magnon entanglement between two massive ferrimagnetic spheres via cavity optomagnonics, Phys. Rev. A **104**, 023711 (2021).

[64] Y.-l. Ren, J.-k. Xie, X.-k. Li, S.-l. Ma, and F.-l. Li, Long-range generation of a magnon-magnon entangled state, Phys. Rev. B **105**, 094422 (2022).

[65] Y. Li, V. G. Yefremenko, M. Lisovenko, C. Trevillian, T. Polakovic, T. W. Cecil, P. S. Barry, J. Pearson, R. Divan, V. Tyberkevych, C. L. Chang, U. Welp, W. K. Kwok, and V. Novosad, Coherent coupling of two remote magnonic resonators mediated by superconducting circuits, Phys. Rev. Lett. **128**, 047701 (2022).

[66] Y. Yang, J. Yao, Y. Xiao, P.-T. Fong, H.-K. Lau, and C.-M. Hu, Anomalous long-distance coherence in critically driven cavity magnonics, Phys. Rev. Lett. **132**, 206902 (2024).

[67] Y.-P. Wang, J. W. Rao, Y. Yang, P.-C. Xu, Y. S. Gui, B. M. Yao, J. Q. You, and C.-M. Hu, Nonreciprocity and unidirectional invisibility in cavity magnonics, Phys. Rev. Lett. **123**, 127202 (2019).

[68] G.-Q. Zhang, W. Feng, W. Xiong, Q.-P. Su, and C.-P. Yang, Generation of long-lived W states via reservoir engineering in dissipatively coupled systems, Phys. Rev. A **107**, 012410 (2023).

[69] J. Qian, C. H. Meng, J. W. Rao, Z. J. Rao, Z. An, Y. Gui, and C.-M. Hu, Non-Hermitian control between absorption and transparency in perfect zero-reflection magnonics, Nat. Commun. **14**, 3437 (2023).

[70] T. Yu, J. Zou, B. Zeng, J. W. Rao, and K. Xia, Non-Hermitian topological magnonics, Phys. Rep. **1062**, 1 (2024).

[71] Z.-Q. Wang, Y.-P. Wang, J. Yao, R.-C. Shen, W.-J. Wu, J. Qian, J. Li, S.-Y. Zhu, and J. Q. You, Giant spin ensembles in waveguide magnonics, Nat. Commun. **13**, 7580 (2022).

[72] X. Wang, Q.-Y. Qiu, K.-W. Huang, and H. Xiong, Nonreciprocal single-photon scattering in giant-spin-ensemble–waveguide magnonics, Phys. Rev. A **108**, 063715 (2023).

[73] R. Huang, Ş. K. Özdemir, J.-Q. Liao, F. Minganti, L.-M. Kuang, F. Nori, and H. Jing, Exceptional photon blockade: Engineering photon blockade with chiral exceptional points, Laser Photonics Rev. **16**, 2100430 (2022).

[74] Y. Zuo, R. Huang, L.-M. Kuang, X.-W. Xu, and H. Jing, Loss-induced suppression, revival, and switch of photon blockade, Phys. Rev. A **106**, 043715 (2022).

[75] A. Ben-Asher, A. I. Fernández-Domínguez, and J. Feist, Non-Hermitian anharmonicity induces single-photon emission, Phys. Rev. Lett. **130**, 243601 (2023).

[76] J. R. Johansson, P. D. Nation, and F. Nori, QuTiP: An open-source Python framework for the dynamics of open quantum systems, Comput. Phys. Commun. **183**, 1760 (2012).

[77] M. Kounalakis, G. E. W. Bauer, and Y. M. Blanter, Analog quantum control of magnonic cat states on a chip by a superconducting qubit, Phys. Rev. Lett. **129**, 037205 (2022).

[78] H. Huebl, C. W. Zollitsch, J. Lotze, F. Hocke, M. Greifenstein, A. Marx, R. Gross, and S. T. B. Goennenwein, High cooperativity in coupled microwave resonator ferrimagnetic insulator hybrids, Phys. Rev. Lett. **111**, 127003 (2013).

[79] R. G. E. Morris, A. F. van Loo, S. Kosen, and A. D. Karenowska, Strong coupling of magnons in a YIG sphere to photons in a planar superconducting resonator in the quantum limit, Sci. Rep. **7**, 11511 (2017).

[80] Y. Li, W. Zhang, V. Tyberkevych, W. K. Kwok, A. Hoffmann, and V. Novosad, Hybrid magnonics: Physics, circuits, and applications for coherent information processing, J. Appl. Phys. **128**, 130902 (2020).

[81] P. G. Baity, D. A. Bozhko, R. Macêdo, W. Smith, R. C. Holland, S. Danilin, V. Seferai, J. Barbosa, R. R. Peroor, S. Goldman, U. Nasti, J. Paul, R. H. Hadfield, S. McVitie, and M. Weides, Strong magnon-photon coupling with chip-integrated YIG in the zero-temperature limit, Appl. Phys. Lett. **119**, 033502 (2021).

[82] S. Guo, D. Russell, J. Lanier, H. Da, P. C. Hammel, and F. Yang, Strong on-chip microwave photon-magnon coupling using ultralow-damping epitaxial $Y_3Fe_5O_{12}$ films at 2 K, Nano Lett. **23**, 5055 (2023).

[83] A. Ghirri, C. Bonizzoni, M. Maksutoglu, A. Mercurio, O. Di Stefano, S. Savasta, and M. Affronte, Ultrastrong magnon-photon coupling achieved by magnetic films in contact with superconducting resonators, Phys. Rev. Appl. **20**, 024039 (2023).

[84] X. Zhang, C.-L. Zou, L. Jiang, and H. X. Tang, Strongly coupled magnons and cavity microwave photons, Phys. Rev. Lett. **113**, 156401 (2014).

[85] M. Goryachev, W. G. Farr, D. L. Creedon, Y. Fan, M. Kostylev, and M. E. Tobar, High-cooperativity cavity QED with magnons at microwave frequencies, Phys. Rev. Appl. **2**, 054002 (2014).

[86] Y. Liu, D. Yang, F. Chai, Y. Xu, F. Cui, and X.-T. Xie, Optical sideband generation in a nonlinear-magnon-mediated cavity, Phys. Rev. A **109**, 013703 (2024).

[87] D.-W. Liu, Y. Wu, and L.-G. Si, Magnon cat states induced by photon parametric coupling, Phys. Rev. Appl. **21**, 044018 (2024).

[88] I.-C. Hoi, C. M. Wilson, G. Johansson, T. Palomaki, B. Peropadre, and P. Delsing, Demonstration of a single-photon router in the microwave regime, Phys. Rev. Lett. **107**, 073601 (2011).

[89] M. Mirhosseini, E. Kim, X. Zhang, A. Sipahigil, P. B. Dieterle, A. J. Keller, A. Asenjo-Garcia, D. E. Chang, and O. Painter, Cavity quantum electrodynamics with atom-like mirrors, Nature (London) **569**, 692 (2019).

[90] Y.-X. Zhang, C. R. i Carceller, M. Kjaergaard, and A. S. Sørensen, Charge-noise insensitive chiral photonic interface for waveguide circuit QED, Phys. Rev. Lett. **127**, 233601 (2021).

[91] X. Gu, A. F. Kockum, A. Miranowicz, Y. Liu, and F. Nori, Microwave photonics with superconducting quantum circuits, Phys. Rep. **718–719**, 1 (2017).

[92] A. Blais, A. L. Grimsmo, S. M. Girvin, and A. Wallraff, Circuit quantum electrodynamics, Rev. Mod. Phys. **93**, 025005 (2021).